# Comprehensive Investigation of the Resolver's Eccentricity Effect on the Field-oriented Control of PMSM

M.S. KhajueeZadeh, M. Emadaleslami, Student Member, IEEE, F. Tootoonchian, Senior Member, IEEE, A. Daniar, Student Member, IEEE, M. C. Gardner, Member, IEEE, B. Akin, Fellow Member, IEEE

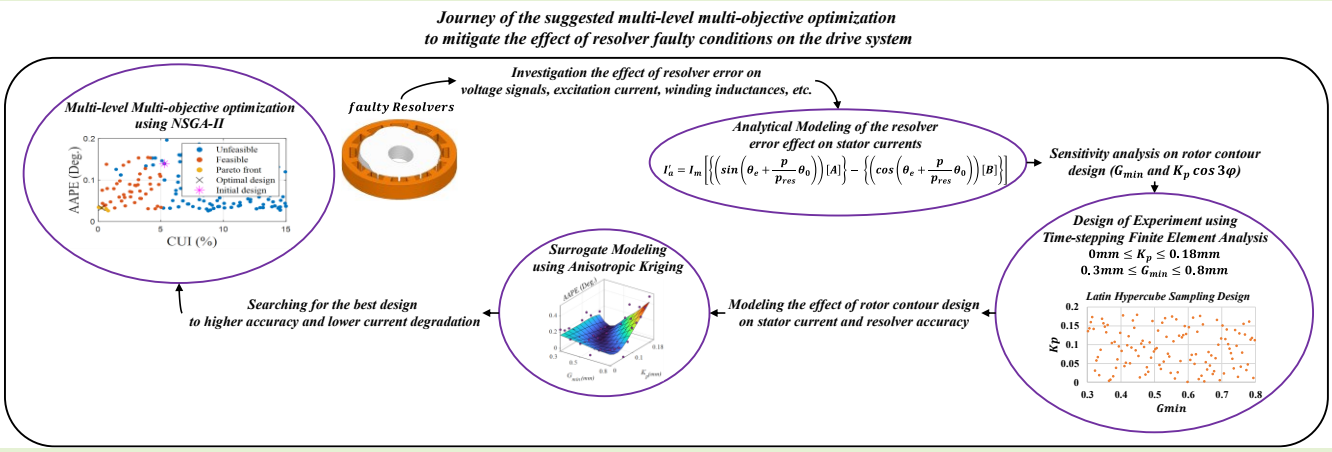


***Abstract*— Accurate position feedback from a resolver is highly critical for high-performance field-oriented control (FOC) drives, and eccentricity in resolvers negatively affects the drive performance. The current unbalance intensity (CUI) of permanent magnet synchronous motors (PMSM) is a known criterion to evaluate drive stability and can be caused by position feedback error. In this paper, the eccentric resolver operation is comprehensively investigated, and the corresponding CUI is analytically evaluated. Accordingly, the error limit is defined for an acceptable operation under eccentricity without derating the motor control. For this purpose, the relationship between the (a) resolver's physical geometry, (b) magnitude and the angle of the stator current, and (c) resolver accuracy are presented through surrogate modeling. Using the proposed analytical current model, the resolver geometry is updated in order to improve the eccentricity tolerance and accuracy and lower the CUI. An optimized rotor design is built, and its accuracy and effect on CUI mitigation are experimentally verified.**

***Index Terms*— Eccentricity, Current Unbalance, Permanent Magnet Synchronous Motor (PMSM), Field Oriented Control (FOC), Resolver, Rotor Angle Error, Surrogate Modeling.**

## I. Introduction

PERMANENT magnet synchronous motors (PMSMs) are highly attractive due to their high efficiency and power density [1]. Position sensors such as hall-effect sensors, encoders, and resolvers are used for high performance PMSM control [2]. Among these, hall-effect sensors are relatively inexpensive yet provide very poor resolution [3]. Encoders have high accuracy and moderate costs, but their accuracy is significantly degraded in nonideal environments due to their sensitive and fragile physical construction [4], which limits their applicability for electric vehicles (EVs). Thus, resolvers are more attractive due to their high precision and resilience to extreme warmth, dust, moisture, noise, and vibrations [1].

Variable reluctance (VR) resolvers are most commonly used for EVs due to their simple rotor structure and lack of brushes and slip rings [5]. The resolver's rotor is mounted on the motor's shaft, while the resolver's stator can be integrated to the motor stator. Thus, any faulty condition in the motor will have a negative effect on the resolver, regardless of whether it

M. S. KhajueeZadeh, is with Electrical Engineering Department, Sharif University of Technology, Tehran, Iran (e-mail: mohammadkhajouie@ee.sharif.edu).

M. Emadaleslami is with Electrical and computer Engineering Department, Tarbiat Modares University, Tehran, Iran (e-mail: mahdi.emadaleslami@modares.ac.ir).

F. Tootoonchian is with Electrical Engineering Department, Iran University of Technology, Tehran, Iran, (email: tootoonchian@iust.ac.ir).

A. Daniar, M. C. Gardner, and B. Akin are with Electrical Engineering Department, The University of Texas at Dallas, Richardson, TX, (email: Ahmad.Daniar@utdallas.edu, Matthew.Gardner@utdallas.edu, Bilal.Akin@utdallas.edu).

results from aerodynamic, electromagnetic, or electrical sources [6]. Eccentricity has the largest effect on resolver accuracy among its fault categories, as it can significantly affect the flux density in the air gap and the magnetic behavior of the resolver [1]. Additionally, excessive vibrations resulting from eccentricity can further degrade resolver accuracy. Static eccentricity can be observed even in brand-new electric machines due to manufacturing or installation imperfections, which results in a bent shaft, bearing wear out, and finally dynamic eccentricity [5]. Static eccentricity results when the stator axis is displaced relative to the rotor and rotation axes. Displacing the rotor axis relative to the stator and rotation axes leads to dynamic eccentricity [7]. The impacts of eccentricity on resolver accuracy have been previously evaluated [7], [8], but the impact of rotor angle error on the drive control performance has not been investigated. Since the resolver error can significantly degrade the drive control stability, it should be evaluated in conjunction with the resolver error.

The mitigation and diagnosis of rotor angle errors in PMSM drives, and the impacts on the motor performance, efficiency and DC-link voltage oscillations are reported in [9]. However, when evaluating the impacts of rotor angle error, the error is often chosen arbitrarily, rather than being linked to the error of a particular sensor [9], [10], [11], [12]. As these studies have largely considered faults that produce a relatively small error, the effect of rotor angle error is negligible in the constant-flux region. These studies were in the field-weakening region, where rotor angle error effect has a more significant impact [10], [11], [12]. The current unbalance (CU) in PMSM drives caused by the rotor angle error is not covered by the previous studies. A CU leads to higher losses and temperature, which can damage the winding insulation and reduce efficiency.

Numerous algorithms are used in motor drive control systems to mitigate the effect of rotor angle error, such as polynomial estimation [13] and minimizing direct-quadrature ($dq$) axis currents [14]. Also, the resolver nonidealities in healthy conditions are usually considered by resolver to digital converter (RDC) algorithms for improving its signal voltages and drive stability [15]. The rotor angle error diagnosis in PMSM control is commonly based on the faulty sensor signals [7] or the stator currents [16]. However, it is also important to predict the impacts of rotor angle error on drive performance. Additionally, designing a resolver with high tolerance for nonidealities could be more effective than implementing a control algorithm to mitigate the effect of the errors. Accordingly, numerous configurations have been suggested and designed to improve resolver accuracy, especially in faulty conditions [17], [18]. However, simultaneously considering the resolver error effects on the motor control drive system yields a more effective design, which was previously neglected.

This paper investigates the effect of faulty resolver conditions on the excitation current, the signal voltages, and its accuracy. Then, the resolver rotor angle error effect on stator currents and CU is investigated analytically and comprehensively. This analytical modeling enables a more straightforward analysis of resolver fault effects. Thus, it can be used for optimizing the resolver configuration by considering the faulty conditions and current unbalance intensity (CUI) in the PMSM drive system. For this purpose, surrogate modeling is used to show the connection between (1) resolver physical geometry, (2) the magnitude and angle of the stator currents, and (3) resolver accuracy. Then, this surrogate model is used in a Multi-Objective Surrogate-Based Optimization (MOSBO) to choose an optimal resolver rotor contour. In order to validate the proposed concept, the designed rotor contour is manufactured, and its accuracy and effect on stator currents CU mitigation are verified experimentally.

## II. Resolver Faulty Conditions Analysis

Theoretically, the winding inductances should be pure sinusoids. However, in practice and especially in resolver eccentricity conditions, nonidealities will emerge in the windings inductances. Thus, the self inductance of the excitation winding ($L_e$) and the mutual inductances between the excitation windings and the signal windings ($M_{\gamma e}$) of the resolver windings can be written as Fourier series as [2]

$$\begin{cases} L_e(\theta_r) = L_{e0} + \sum L_{en} \sin(n[\theta_r - \theta_0] + \varphi_{en}) \\ M_{se}(\theta_r) = M_{s0} + \sum M_{sn} \sin(n[\theta_r - \theta_0] + \varphi_{sn}) \\ M_{ce}(\theta_r) = M_{c0} + \sum M_{cn} \cos(n[\theta_r - \theta_0] + \varphi_{cn}) \end{cases} \quad (1)$$

where $\theta_0$ is the rotor angle shifting, the Fourier series coefficients are $L_{e0}$, $M_{s0}$, $M_{c0}$, $L_{en}$, $M_{sn}$, and $M_{cn}$ and the Fourier series angles are $\varphi_{en}$, $\varphi_{sn}$, and $\varphi_{cn}$. Moreover, $\theta_r$ is the electric rotor angle of resolver. The signal currents are negligible compared to the excitation current, so the flux linkages can be rewritten as [2]

$$\begin{cases} \lambda_e = L_e(\theta_r) i_e \\ \lambda_{s/c} = M_{se/ce}(\theta_r) i_e \end{cases} \quad (2)$$

where $\lambda_\gamma$ is the flux linkage and $i_e$ is the excitation current. Then, the signal voltages are written as:

$$v_{s/c} = d\lambda_{s/c}/dt \quad (3)$$

where $v_s$ and $v_c$ are the sine and cosine signal voltages, respectively. As the excitation windings are fed by a high-frequency AC voltage; the excitation current and voltage are written as

$$\begin{cases} i_e = (v_e - d\lambda_e/dt)/R_e \\ v_e = v_m \cos \omega_{ex} t \end{cases} \quad (4)$$

where $R_e$ is the excitation winding resistance and $v_e$ is the excitation voltage. Additionally, as $L_e(\theta_r)$ is approximately constant [2], $d\big(L_e(\theta_r)\big)/d\theta_r = 0$ holds. Thus, $i_e$ can be written as (5) [19], where $i_{me}$ is the magnitude and $\alpha_e$ the phase angle of $i_e$. Substituting (5) into (2) for calculating (3) leads to (6) [19]. As the faulty resolver conditions will lead to resolver signal voltages degradation, (6) is rewritten as (7). For the sake of simplicity, the effect of signal voltage degradations is investigated separately and independently through RDC [20]. A summary of the above degradations' effect on revolver signal voltages and rotor angle extraction is given in Table I, where $A_1$

$$i_e(t) = v_m \cos\left(\omega_{ex}t - \tan^{-1}\left(\frac{L_e\omega_e}{R_e}\right)\right) / \sqrt{{R_e}^2 + (L_e\omega_e)^2} = i_{me}\cos(\omega_{ex}t - \alpha_e) \tag{5}$$

$$\begin{cases} v_s = d\lambda_s/dt = d(M_{se} \times i_e)/dt \approx M_{se}d(i_e)/dt = [-i_{me}\omega_{ex}\sin(\omega_{ex}t - \alpha_e)] \times [M_{s0} + \sum M_{sn}\sin(n[\theta_r - \theta_0] + \varphi_{sn})] \\ v_c = [-i_{me}\omega_{ex}\sin(\omega_{ex}t - \alpha_e)] \times [M_{c0} + \sum M_{cn}\cos(n[\theta_r - \theta_0] + \varphi_{cn})] \end{cases} \tag{6}$$

$$\begin{cases} v_s = Kv_m\left[\frac{k1}{k} + A_1\sin(\theta_r) + \sum_{n=1}^{\infty} B_n\sin(n[\theta_r - \theta_0] + \varphi_{sn})\right]\sin(\omega_e t - \alpha_e) \\ v_c = Kv_m\left[\frac{k2}{k} + A_1(1+\zeta)\cos(\theta_r + \xi) + \sum_{n=1}^{\infty} B_n\cos(n[\theta_r - \theta_0] + \varphi_{cn})\right]\sin(\omega_e t - \alpha_e) \end{cases} \tag{7}$$

TABLE I
FAULTY CONDITION EFFECTS ON SIGNAL VOLTAGE DEGRADATION

| Type of non-ideality | Demodulated signal voltages degradation | Position error harmonic |
|---|---|---|
| Undesirable Harmonics | $\begin{cases} u_s = [A_1\sin(\theta_r) + B_n\sin(n\theta_r)] \\ u_c = [A_1\cos(\theta_r) + B_n\cos(n\theta_r)] \end{cases}$ | $\tilde{\theta} \approx \left(\frac{B_n}{A_1}\right)\sin((n-1)\theta_r)$ |
| Amplitude Imbalance | $\begin{cases} u_s = \sin\theta_r \\ u_c = (1+\zeta)\cos\theta_r \end{cases}$ | $\tilde{\theta} \approx -\frac{\zeta}{2}\sin 2\theta_r$ |
| Imperfect Quadrature | $\begin{cases} u_s = \sin\theta_r \\ u_c = \cos(\theta_r + \xi) \end{cases}$ | $\tilde{\theta} \approx \frac{\xi}{2}(1 - \cos 2\theta_r)$ |
| DC Offset | $\begin{cases} u_s = [\frac{k1}{k} + \sin\theta_r] \\ u_c = [\frac{k2}{k} + \cos\theta_r] \end{cases}$ | $\tilde{\theta} \approx \sqrt{2}\frac{k0}{k}\cos\left(\theta_r + \frac{\pi}{4}\right)$ |

is main order of $u_s$, $B_n$ are the Fourier series coefficients, $K$ is the transformer coefficient, $\zeta$ is the effect of magnitude inequality, $\xi$ is the effect of the angle shifting not being exactly 90 degrees, and $\frac{k1}{k}$ and $\frac{k2}{k}$ are DC offset effects.

In the following study, a 1-X VR resolver with a constant turn non-overlapping winding (CTNOW) configuration is evaluated. The maximum and minimum airgaps are $G_{max} = 2$ mm and $G_{min} = 0.5$ mm, respectively. The considered resolver is shown in Fig. 1. Using a 1-X resolver provides advantages, such as absolute rotor position information and compatibility with a wide range of motor pole numbers. The odd harmonic orders of signal voltages emerge even in healthy conditions, and faulty conditions intensify their magnitude [8]. On the contrary, the even harmonic orders will emerge exclusively when the fault occurs [8]. Thus, the eccentricity will cause the intensifying of the 3rd and 5th orders and the emergence of the 2nd order in signal voltages [18]. Moreover, the DC offset was shown to be a symptom of eccentricity [7]. According to Table I, the above harmonic orders of signal voltage will lead to 1st, 2nd, and 4th harmonic orders ($\theta_1$, $\theta_2$, and $\theta_4$) in the rotor angle error, $\tilde{\theta}$, while their magnitude also has a dependency on $A_1$ [7].

## III. ANALYTICAL MODELING OF THE STATOR CURRENTS IN PMSM DRIVE UNDER RESOLVER FAULTY CONDITIONS

If the severity of the faulty resolver condition is significant, the CU of the PMSM can be nonnegligible, which can produce variations in the armature magnetic field and reduce efficiency. The CUI can be analyzed using the positive, negative, and zero sequence currents ($I_{P,N,0}$). With an ungrounded Y connection in the stator windings, $I_0$ can be neglected [21]. Thus, by applying the Fortescue transform, the above symmetrical currents can be written as follows, where $\alpha = exp\left(\frac{2\pi}{3}j\right)$:

$$[I_P\ I_N]^T = \frac{1}{3}\begin{bmatrix} 1 & \alpha & \alpha^2 \\ 1 & \alpha^2 & \alpha \end{bmatrix}[I_a\ I_b\ I_c]^T \tag{8}$$

In healthy resolver conditions, the main order of the current has a higher effect on the current magnitude and angle. Thus, using a satisfactory estimate, CUI can only be investigated in conjunction with degeneration of the main order of the stator currents. Thus, the ideal stator currents ($I_{a,b,c}$) will be written as

$$\begin{cases} I_a = I_m\sin(\theta_e) \\ I_b = I_m\sin(\theta_e - 2\pi/3). \\ I_c = I_m\sin(\theta_e + 2\pi/3) \end{cases} \tag{9}$$

where $I_m$ is the current magnitude and $\theta_e$ is the electric rotor angle of the motor. Applying the Park transform gives *d-q* currents ($I_{d,q}$), according to the shown rotating reference frames in Fig. 2.

$$[I_d\ I_q]^T = \frac{2}{3}T(\theta_e)[I_a\ I_b\ I_c]^T \tag{10}$$

$$T(\theta_e) = \begin{bmatrix} \cos(\theta_e) & \cos\left(\theta_e - \frac{2\pi}{3}\right) & \cos\left(\theta_e + \frac{2\pi}{3}\right) \\ -\sin(\theta_e) & -\sin\left(\theta_e - \frac{2\pi}{3}\right) & -\sin\left(\theta_e + \frac{2\pi}{3}\right) \end{bmatrix} \tag{11}$$

$$[I_d \quad I_q] = [0 \quad -I_m] \tag{12}$$

The resolver's faulty conditions will generate nonidealities in

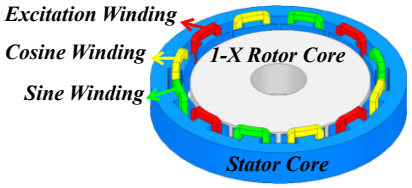


Fig. 1. Schematic of the investigated 1-X VR resolver with CTNOW.

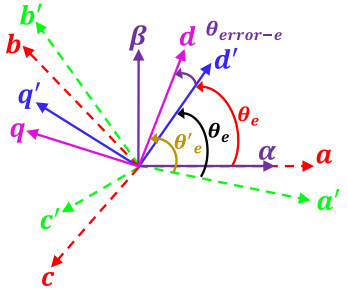


Fig. 2. Field orientation inaccuracy caused by rotor angle error, where the symbols without primes indicate the ideal reference frames, whereas the primed symbols indicate the degraded reference frame estimations with the faulty resolver.

the stator currents. Accordingly, using the inverse Park transform, the stator currents are rewritten as

$$[I_a' \; I_b' \; I_c']^T = T(\theta_e')^T [I_d \; I_q]^T \tag{13}$$

$$T(\theta_e')^T = \begin{bmatrix} \cos(\theta_e') & -\sin(\theta_e') \\ \cos\left(\theta_e' - \frac{2\pi}{3}\right) & -\sin\left(\theta_e' - \frac{2\pi}{3}\right) \\ \cos\left(\theta_e' + \frac{2\pi}{3}\right) & -\sin\left(\theta_e' + \frac{2\pi}{3}\right) \end{bmatrix} \tag{14}$$

For the sake of brevity, $I_a'$ is chosen as a criterion for the following examinations.

$$I_a' = I_m \sin(\theta_e'), \tag{15}$$

where, according to Fig. 2,

$$\theta_e' = \theta_e + \theta_{Error-e}, \tag{16}$$

where $\theta_e$ is ideal electric rotor angle of the primary motor, $\theta_{Error-e}$ is rotor angle error of the primary motor, and $\theta_e'$ is degraded rotor angle determined from the faulty resolver. Differences in pole numbers between the motor and resolver ($p_{res} \neq p$) is regarded as a coefficient in electric rotor angle,

$$\begin{cases} p_{res}\theta_e/p = \theta_r \\ p_{res}\theta_{Error-e}/p = \tilde{\theta} \end{cases} \tag{17}$$

(For this study, $p_{res}$ is 1, and $p$ is 2.) Moreover, according to the intrinsic periodicity of the resolver, $\theta_{Error-e}$ can be written as the Fourier series in (18). By referring to (15), $\sin(\theta_e')$ must be rewritten for calculating $I_a'$ through (16)-(18), as (19)-(20). Using Taylor's trigonometric theorem, (20) will be rewritten. Thereby, substituting (20) into (19) and calculating (15) gives (21). Using a satisfactory estimate, the investigation of CUI can only be on the degradation of the main order of stator currents. Details are given in Appendix for more clarity. Similar comprehensive evaluations can be performed for $I_b'$ and $I_c'$. Then, the CUI indicates the degradation of stator currents and can be written as the ratio of negative sequence current ($I_N$) to positive sequence current ($I_P$),

$$CUI = \left|\frac{I_N}{I_P}\right| \times 100\% \,. \tag{22}$$

The above analytical modeling is an efficient tool for improving resolver accuracy and improving fault tolerance. It also provides a simpler resolver fault effect analysis for PMSM stator currents and CUI, which often requires more complex and time-consuming analyses involving the drive system.

## IV. Surrogate-Based Resolver Optimization in Faulty Condition

### A. Methodology

In the case of resolver geometric design, as shown in [2], a slight change in resolver geometry, especially the rotor contour of the VR resolver, can significantly affect resolver accuracy. However, evaluating a large number of designs with finite element analysis (FEA) is time-consuming, especially when also evaluating the CUI in the PMSM drive system. By employing the analytical modeling in (21), the drive system can be removed from the model, speeding up the simulations. Nonetheless, it is still quite time-consuming simply to evaluate a large number of resolver geometries with FEA, so surrogate modeling can be used as a faster alternative. The methodology of surrogate modeling has three stages, including design of experiments (DOE), surrogate model training, and validation [22].

In this study, DOE was generated using optimal Latin hypercubes sampling designs (OLHSD) to gain the maximum insight into the design with the fewest FEA simulations [23]. In the training stage, the anisotropic Kriging modeling was employed due to its higher accuracy than response surface methodology (RSM) and lower complexity than an artificial neural network (ANN) [24]. Accordingly, six Kriging surrogate models (SMs) are trained to estimate the magnitude and the angle of the degraded stator currents, along with one Kriging SM for estimating average of absolute position error (AAPE) in faulty resolver conditions. Surrogate modeling provides the connection between the degraded stator currents and the resolver geometry. FEA and the analytical model in (21) are used to generate the training dataset. After training, the SMs can be applied to evaluate many resolver geometries.

The surrogate modeling in this study focuses on changing the resolver rotor contour in a 1-X VR resolver, considering the stator geometry and winding configuration fixed. In VR resolvers, the air-gap length ($\delta$) varies as follows [17]:

$$\delta = \frac{G_{min}G_{max}}{(G_{min} + G_{max}) + (G_{min} - G_{max})\cos\varphi} \tag{23}$$

$$\theta_{Error-e} = p_{res}\tilde{\theta}/p = p_{res}\theta_0/p + \sum_{N=1}^{\infty} p_{res}\theta_N \sin(Np_{res}\theta_e/p + \varphi_N)/p \tag{18}$$

$$\sin(\theta_e') = \sin(\theta_e + \theta_{Error-e}) = \sin(\theta_e)\cos(\theta_{Error-e}) + \cos(\theta_e)\sin(\theta_{Error-e}) \tag{19}$$

$$\begin{cases} \cos(\theta_{Error-e}) = \cos(p_{res}\theta_0/p + \sum_{N=1}^{\infty} p_{res}\theta_N \sin(Np_{res}\theta_e/p + \varphi_N)/p) \\ \sin(\theta_{Error-e}) = \sin(p_{res}\theta_0/p + \sum_{N=1}^{\infty} p_{res}\theta_N \sin(Np_{res}\theta_e/p + \varphi_N)/p) \end{cases} \tag{20}$$

$$I_a' = I_m\left[\left\{\left(\sin\left(\theta_e + \frac{p}{p_{res}}\theta_0\right)\right)[A]\right\} - \left\{\left(\cos\left(\theta_e + \frac{p}{p_{res}}\theta_0\right)\right)[B]\right\}\right]$$
$$A = 1 - \sum_{N=1}^{\infty}\left(\frac{\left(\frac{p}{p_{res}}\theta_N\right)^2}{4}\right) + \left(\frac{\left(\frac{p}{p_{res}}\theta_N\right)^2}{4}\right)\cos\left(2N\frac{p_{res}\,\theta_e}{p} + 2\varphi_N\right) \tag{21}$$

$$B = \sum_{N=1}^{\infty}\frac{p}{p_{res}}\theta_N \sin\left(N\frac{p_{res}\,\theta_e}{p} + \varphi_N\right) - \frac{\left(\frac{p}{p_{res}}\theta_N\right)^3}{6}\left(\frac{3}{4}\right)\sin\left(N\frac{p_{res}\,\theta_e}{p} + \varphi_N\right) + \frac{\left(\frac{p}{p_{res}}\theta_N\right)^3}{6}\left(\frac{1}{4}\right)\sin\left(3N\frac{p_{res}\,\theta_e}{p} + 3\varphi_N\right)$$

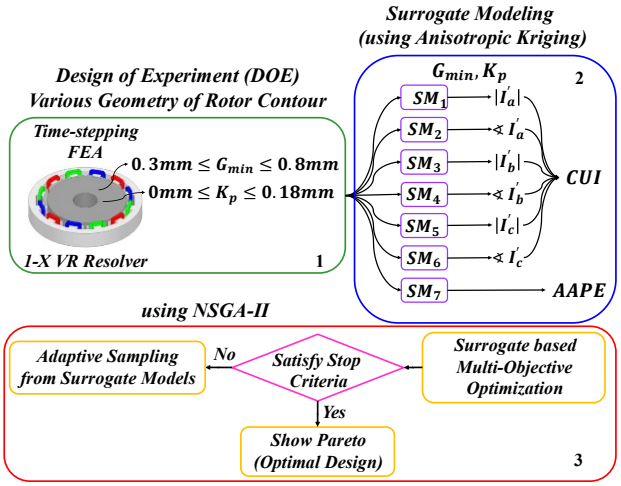


Fig. 3. Procedure for the employed multi-objective surrogate-based optimization (MOSBO), including design of experiments (DOE), surrogate modeling, and NSGA-II.

where $\varphi$ is the angular coordinate, $G_{min}$ is the minimum air-gap length and $G_{max}$ is the maximum air-gap length. As shown, the eccentricity has the effect of intensifying the 3rd and 5th orders and producing the 2nd order of the signal voltages. According to [2], mitigating the 3rd order will be most effective in improving resolver accuracy. So, (23) can be rewritten as below [25]:

$$\delta = \frac{G_{min}G_{max}}{(G_{min}+G_{max})+(G_{min}-G_{max})\cos\varphi - K_p\cos 3\varphi} \tag{24}$$

where $K_p$ is the coefficient of injected 3rd order. Besides $K_p$, the variation of $G_{min}$ can affect accuracy. In our study, $G_{max}$ will be constant at the same value as the initial design, 2 mm. Consequently, the training dataset will be based on varying $G_{min}$ and $K_p$ in the 1-X VR resolver rotor contour. Fig. 3 gives a summary of the DOE, surrogate modeling, and optimization using the evolutionary non-dominated sorting genetic algorithm II (NSGA-II).

TABLE II
VALIDATION OF THE TRAINED SURROGATE MODELS

| Surrogate Model | R-Squared ($R^2$) | Mean Normalized Error (MNE) |
|---|---|---|
| AAPE | 0.996 | 0.00136 |
| $\lvert I'_a\rvert$ | 0.995 | 0.00184 |
| $\measuredangle I'_a$ | 0.970 | 0.00278 |
| $\lvert I'_b\rvert$ | 0.998 | 0.00107 |
| $\measuredangle I'_b$ | 0.999 | 0.00025 |
| $\lvert I'_c\rvert$ | 0.986 | 0.00297 |
| $\measuredangle I'_c$ | 0.999 | 0.00020 |

## B. Results and Discussion

The variation range of $G_{min}$ and $K_p$ in the DOE must be chosen carefully to cover all of the possible individuals in the design space. As shown in Fig. 3, $G_{min}$ varies from 0.3 mm to 0.8 mm and $K_p$ from 0 mm to 0.18 mm. Accordingly, using OLHSD and 2D FEA, alongside the analytical model in (21), 120 geometries were evaluated to obtain the AAPE, the magnitudes of the degraded stator currents, and the angles of degraded stator currents in the eccentric condition (0.1 mm static eccentricity).

### B.1. Surrogate Modeling and Efficiency analysis

After dividing the DOE into training and test sets with a ratio of 80% to 20%, using the training set along with the anisotropic Kriging algorithm gives the SMs, with the results displayed in Fig. 4. Two accuracy metrics, R-Squared ($R^2$) and Mean Normalized Error (MNE), are employed to assess the SMs using the test set. Table II shows that the SMs have significant accuracy in predicting the AAPE metric and the magnitude and angle of degraded stator currents, as the $R^2$ score is approximately 1 and the MNE is near zero.

### B.2. Surrogate-based Multi-objective Optimization

The NSGA-II algorithm aims to identify the rotor contour designs optimally based on the minimum value of the two objectives, CUI and AAPE, within the design and drive constraints, as shown below

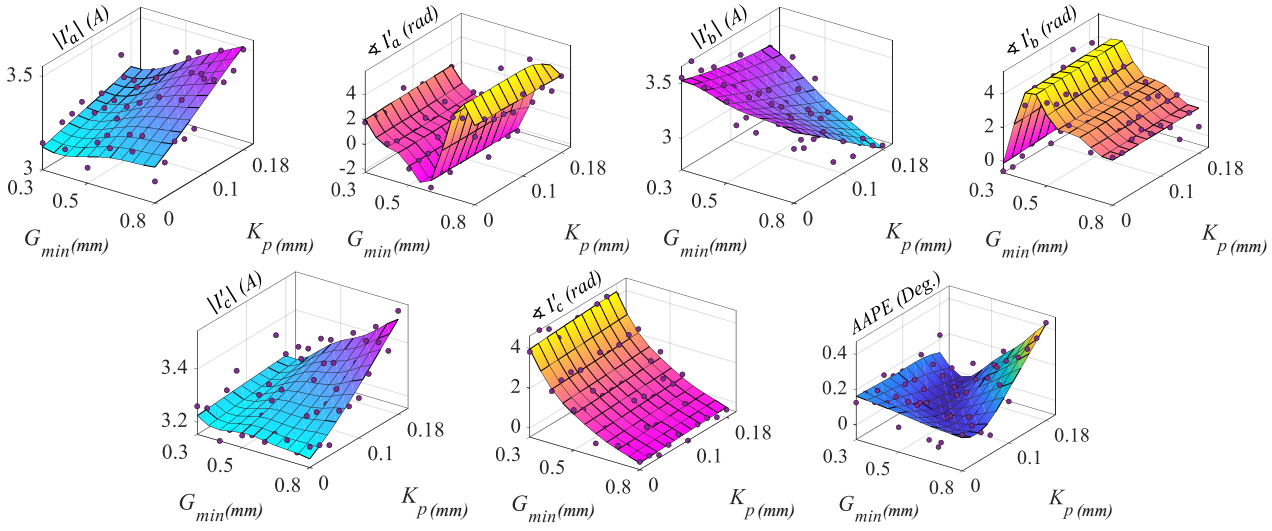


Fig. 4. The trained Surrogate Models (SMs) for AAPE and stator currents degradation.

$$F_{min} = \left( \frac{CUI_{final\ design}}{CUI_{initial\ design}}, \frac{AAPE_{final\ design}}{AAPE_{initial\ design}} \right) \tag{25}$$

$$\min_{G_{min}, K_p} F_{min} \quad s.t: \begin{cases} 0.3 \text{ mm} < G_{min} < 0.8 \text{ mm} \\ 0 \text{ mm} < K_p < 0.18 \text{ mm} \\ CUI < 5\% \\ AAPE < 0.5 \text{ deg.} \\ |\theta_{Ia} - \theta_{Ib}| + |\theta_{Ia} - \theta_{Ic}| + |\theta_{Ib} - \theta_{Ic}| = \frac{8\pi}{3} \end{cases} \tag{26}$$

where the fifth constraint guarantees the 120 degrees of phase-shifting between stator currents. Accordingly, 10,000 designs, including 20 generations of 500 individuals each, were generated before the algorithm converged. Fig. 5 shows the CUI and AAPE of the designs. In the initial design, the $G_{min}$, $K_p$, AAPE, and CUI values were 0.5 mm, 0 mm, 0.1394 deg., and 5.2%, respectively, with the 0.1 mm static eccentricity. The final design, which is chosen from the Pareto front according to (25), achieved $G_{min}$, $K_p$, AAPE, and CUI values of 0.5 mm, 0.09 mm, 0.033 deg., and 0.2662%, respectively, with the 0.1 mm static eccentricity. Fig. 6 illustrates the AAPE and CUI of the final design.

Inverter-driven machines commonly have a 5% CUI constraint, according to the derating condition of the drive [26]. Thus, the CUI constraint can be used to limit the eccentricity percentages that are acceptable.

### *B.3. Computational Cost*

Designing the resolver to obtain higher accuracy and fault tolerance can be quite time-consuming. Moreover, considering the impact of resolver error on the drive performance can increase complexity and computation time. Each of the 120 designs evaluated via 2D FEA for the DOE required approximately 48 minutes to evaluate using a high-performance computing cluster. Evaluating the impact on drive performance using MATLAB/Simulink requires another 5 minutes per design. On the other hand, by employing the analytical model in (21), the 5-minute evaluation in Simulink can be avoided. Using 2D-FEA for the 10,000 NSGA-II designs would be extraordinarily slow. However, with the surrogate model, the NSGA-II is completed within only 30 minutes including both training the surrogate model and optimization. Considering the above times, taking advantage of the surrogate and analytical models gives a significant time saving (more than 98.92%), as shown in Table III.

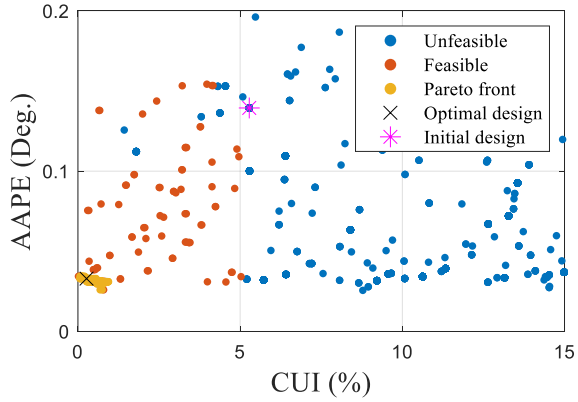


Fig. 5. CUI versus AAPE for the designs generated by the NSGA-II.

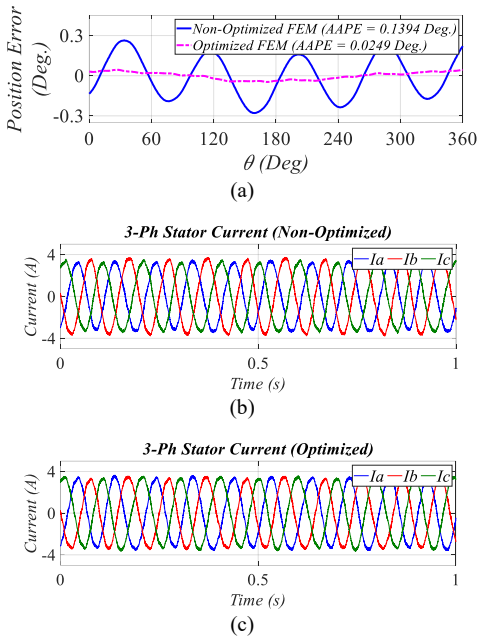


Fig. 6. (a) The position errors of the initial and optimized resolver designs and the drive currents with the (b) initial and (c) optimized resolver designs.

## V. Experimental Measurements

The final design of the rotor contour ($G_{min} = 0.5$ mm, $K_p = 0.09$ mm) was built and tested experimentally in the PMSM drive control system to verify the above analyses. Fig. 7 shows the prototype VR rotor and stator with the CTNOW configuration. The PMSM's technical data is shown in Table IV. A UniDrive SP size 2023 (7.5 KW) is employed to drive the PMSM, while the prototype VR resolver gives the rotor angle and angular velocity feedback. The FOC algorithm is employed for the control strategy, and the inverter's switching frequency is 6 kHz. As the resolver signal voltages processing is necessary to extract the rotor angle and angular velocity, a signal module with 14-bit operating resolution is used along with the UniDrive. The signal module also supplies the excitation winding with a 4 Vrms, 6 kHz sinusoidal signal. The ratio of turn numbers between the signal and excitation windings is 2:1. Before running the drive system, the PMSM and resolver are aligned, so the initial rotor angle error is zero. In order to test the resolver in the faulty condition, 0.1 mm static eccentricity is created in the resolver by modifying the stator frame. As the PMSM by default has an absolute encoder, the accuracy degradation of the resolver under eccentricity can be

TABLE III
Comparison of Computational Cost

| Type of Method | Total Number | Computational Burden (Min.) |
|---|---|---|
| 2D FEA for DOE | 120 | 5,760 |
| 2D FEA for Optimization | 10,000 | 480,000 |
| PMSM drive (SIMULINK) for DOE | 120 | 600 |
| PMSM drive (SIMULINK) for Optimization | 10,000 | 50,000 |
| Analytical Model of Stator Currents | 3 | 3 |
| Surrogate Modeling (Training) | 7 | 7 |
| NSGA-II Algorithm for Optimization | 10,000 | 25 |

Fig. 7. The prototype stator and rotor of the 1-X resolver with CTNOW configuration.

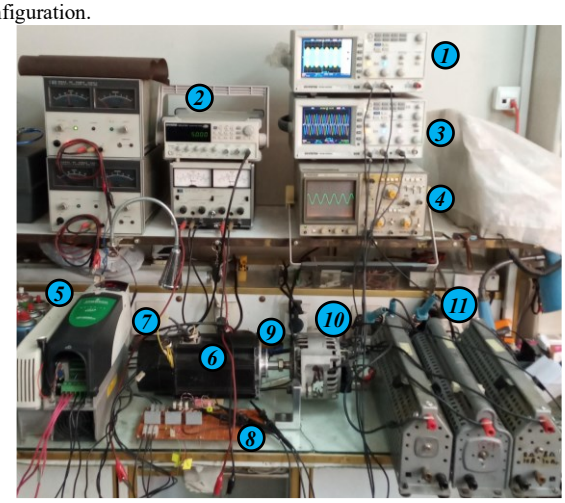


Fig. 8. Experimental test setup: (1) Signal voltages (2) Function generator (3) Degraded stator currents (4) Excitation voltage (5) UniDrive SP (6) PMSM (7) Absolute encoder (8) Current sensors (9) Prototype resolver (10) Generator (11) Resistor loads.

shown by calculating the rotor angle error and the AAPE criterion.

The reference encoder designation is 154SG, with a 24-bit resolution. Due to the significant negative effect of excitation frequency and switching frequency, a low-pass filter (LPF) must be used after the resolver angular velocity feedback to attenuate the high-frequency oscillations. The test bench, including PMSM, drive system, and 1-X VR resolver, is shown in Fig. 8. The signal voltages of the built resolver in healthy and faulty conditions (static eccentricity with 0.1 mm stator movement) are displayed in Fig. 9. Moreover, the stator currents of PMSM are displayed in Fig. 10 under the healthy and faulty conditions of the resolver. The measurements verify that the CUI with the optimized resolver is adequately small (0.0974% and 0.3372% under healthy and eccentric conditions, respectively). Also, the AAPE of the built resolver is 0.042 deg, which agrees with the final design's AAPE (0.033 deg.). Using the peak detection method and MATLAB software to avoid error from the RDC effect, the accuracy of the built resolver was calculated.

## VI. Conclusion

This paper has evaluated the impact of static eccentricity on the resolver accuracy and the resulting impact on PMSM drive performance when using FOC in the constant-flux region. Also, an analytical model for the degraded stator currents resulting from rotor angle errors was introduced to significantly accelerate simulations. Accordingly, the eccentricity constraint in various conditions and movements (dynamic and static eccentricity) were determined to avoid de-rating the drive. The mitigation of CU is critical to avoid excessive heat generation in the stator windings. However, modifying the resolver rotor

TABLE IV
Nominal Technical Data of The Examined PMSM

| PMSM (MAC 071 B-FS) | | | |
|---|---|---|---|
| Designation (Unit) | Values | Designation (Unit) | Values |
| Nominal Speed (rpm) | 1500 | Continuous Torque (Nm) | 4.4 |
| Number of Pole Pairs | 2 | Continuous Current (A) | 5 |
| Windings Inductance (mH) | 22 | Windings Resistance (Ω) | 2.7 |
| Torque Constant (Nm/A) | 0.88 | Permanent Magnet Flux Linkage (Wb) | 0.44 |

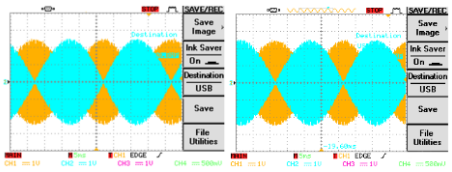

(a) (b)

Fig. 9. Signal voltages of the prototype resolver in both (a) healthy and (b) faulty conditions (0.1 mm static eccentricity).

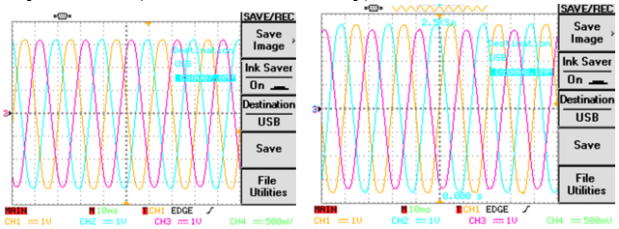

(a) (b)

Fig. 10. Stator currents of the PMSM with both (a) healthy and (b) faulty (0.1 mm static eccentricity) conditions for the prototype resolver.

contour can effectively reduce the CU, even in the presence of eccentricity. Thus, first, highly accurate SMs were developed for quick estimation of the resolver accuracy and stator currents degradation in faulty resolver conditions. Then, the trained SMs were employed in the NSGA-II algorithm to find an optimal resolver design, which has low AAPE, produces minimal CU, and well tolerates eccentricity. Through the surrogate and analytical modeling in this study, the computation time was reduced by about 98.9% relative to using FEA and Simulink to evaluate each design. Finally, the designed resolver was prototyped (rotor contour and stator with CTNOW configuration), and its high accuracy and mitigation of CUI were verified experimentally.

## VII. Appendix

Using the Taylor trigonometric theorem, (20) will be rewritten as (A1)-(A2). Accordingly, by substituting (A1)-(A2) into $\sin(\theta_e')$, $I_a'$ will be written as (21). In this study, $p_{res}$ is 1, and $p$ is 2; so (21) can be rewritten as (A3). Since the investigation of CUI can only be on the degradation of the main order of stator currents, (A3) will be rewritten as (A4).

## References

[1] M. S. Khajueezadeh, S. FeizHoseini, Z. Nasiri-Gheidari, and M. Behzad, "Analysis of Torsional Vibrations on the Resolver Under Eccentricity in PMSM Drive System," *IEEE Sens J*, vol. 22, no. 22, pp. 21592–21599, Nov. 2022, doi: 10.1109/JSEN.2022.3209991.

[2] M. KhajueeZadeh, H. Saneie, and Z. Nasiri-Gheidari, "Development of a Hybrid Reference Model for Performance Evaluation of Resolvers," *IEEE Trans Instrum Meas*, vol. 70, pp. 1–8, 2021, doi: 10.1109/TIM.2021.3097409.

$$\begin{cases}\cos(\theta_{Error-e}) = \cos\left(\frac{\mathrm{p}}{\mathrm{p_{res}}}\theta_0\right)\cos\left(\frac{\mathrm{p}}{\mathrm{p_{res}}}\theta_\mathrm{N}\ \sin\left(\mathrm{N}\frac{\mathrm{p_{res}}\,\theta_\mathrm{e}}{\mathrm{p}}+\ \varphi_\mathrm{N}\right)\right)-\ \sin\left(\frac{\mathrm{p}}{\mathrm{p_{res}}}\theta_0\right)\sin\left(\frac{\mathrm{p}}{\mathrm{p_{res}}}\theta_\mathrm{N}\ \sin\left(\mathrm{N}\frac{\mathrm{p_{res}}\,\theta_\mathrm{e}}{\mathrm{p}}+\ \varphi_\mathrm{N}\right)\right)\\ \sin(\theta_{Error-e}) = \sin\left(\frac{\mathrm{p}}{\mathrm{p_{res}}}\theta_0\right)\cos\left(\frac{\mathrm{p}}{\mathrm{p_{res}}}\theta_\mathrm{N}\ \sin\left(\mathrm{N}\frac{\mathrm{p_{res}}\,\theta_\mathrm{e}}{\mathrm{p}}+\ \varphi_\mathrm{N}\right)\right)-\ \cos\left(\frac{\mathrm{p}}{\mathrm{p_{res}}}\theta_0\right)\sin\left(\frac{\mathrm{p}}{\mathrm{p_{res}}}\theta_\mathrm{N}\ \sin\left(\mathrm{N}\frac{\mathrm{p_{res}}\,\theta_\mathrm{e}}{\mathrm{p}}+\ \varphi_\mathrm{N}\right)\right)\end{cases} \quad (A1)$$

$$\begin{cases}\cos\left(\frac{\mathrm{p}}{\mathrm{p_{res}}}\theta_\mathrm{N}\ \sin\left(\mathrm{N}\frac{\mathrm{p_{res}}\,\theta_\mathrm{e}}{\mathrm{p}}+\ \varphi_\mathrm{N}\right)\right) = 1-\sum_{N=1}^{\infty}\frac{\left(\frac{\mathrm{p}}{\mathrm{p_{res}}}\theta_\mathrm{N}\right)^2\sin\left(\mathrm{N}\frac{\mathrm{p_{res}}\,\theta_\mathrm{e}}{\mathrm{p}}+\varphi_\mathrm{N}\right)^2}{4}\\ \sin\left(\frac{\mathrm{p}}{\mathrm{p_{res}}}\theta_\mathrm{N}\ \sin\left(\mathrm{N}\frac{\mathrm{p_{res}}\,\theta_\mathrm{e}}{\mathrm{p}}+\ \varphi_\mathrm{N}\right)\right) = \sum_{N=1}^{\infty}\frac{\mathrm{p}}{\mathrm{p_{res}}}\theta_\mathrm{N}\sin\left(\mathrm{N}\frac{\mathrm{p_{res}}\,\theta_\mathrm{e}}{\mathrm{p}}+\ \varphi_\mathrm{N}\right)-\frac{\left(\frac{\mathrm{p}}{\mathrm{p_{res}}}\theta_\mathrm{N}\right)^3\sin\left(\mathrm{N}\frac{\mathrm{p_{res}}\,\theta_\mathrm{e}}{\mathrm{p}}+\varphi_\mathrm{N}\right)^3}{6}\end{cases} \quad (A2)$$

$$I_a{}' = I_a' = I_m\left[\left\{\left(\sin\left(\theta_e+\frac{p}{p_{res}}\theta_0\right)\right)[C]\right\}-\left\{\left(\cos\left(\theta_e+\frac{p}{p_{res}}\theta_0\right)\right)[D]\right\}\right]$$
$$C = 1-\sum_{N=1}^{\infty}(\theta_N)^2+(\theta_N)^2\cos(N\theta_e+2\varphi_N) \quad (A3)$$
$$D = \sum_{N=1}^{\infty}\frac{\theta_N}{2}sin\left(\frac{N\theta_e}{2}+\ \varphi_N\right)-(\theta_N)^3\ sin\left(\frac{N\theta_e}{2}+\ \varphi_N\right)+\frac{(\theta_N)^3}{3}sin\left(3\frac{N\theta_e}{2}+\ 3\varphi_N\right)$$

$$I_a{}' = I_m\left[sin\left(\theta_e+\frac{\theta_0}{2}\right)[1-\sum_{N=1}^{\infty}(\theta_N)^2]+\frac{(\theta_2)^2}{2}\ sin\left(-\theta_e+\frac{\theta_0}{2}-2\varphi_2\right)-\frac{\theta_4}{4}sin\left(-\theta_e+\frac{\theta_0}{2}-\varphi_4\right)+\left(\frac{\theta_4}{2}\right)^3\ sin\left(-\theta_e+\frac{\theta_0}{2}-\varphi_4\right)\right] \quad (A4)$$


[3] H. Saneie, Z. Nasiri-Gheidari, and A. Belahcen, "On the Field-Reconstruction Method for Electromagnetic Modeling of Resolvers," *IEEE Trans Instrum Meas*, vol. 72, pp. 1–8, 2023, doi: 10.1109/TIM.2022.3224527.

[4] X. Ge, Z. Q. Zhu, R. Ren, and J. T. Chen, "A Novel Variable Reluctance Resolver with Nonoverlapping Tooth–Coil Windings," *IEEE Transactions on Energy Conversion*, vol. 30, no. 2, pp. 784–794, Jun. 2015, doi: 10.1109/TEC.2014.2377214.

[5] P. Naderi and R. Ghandehari, "Comprehensive Analysis on a New Type VR-Resolver With Toroidal Windings Under Healthy and Eccentric Cases," *IEEE Transactions on Industrial Electronics*, vol. 69, no. 12, pp. 13754–13762, Dec. 2022, doi: 10.1109/TIE.2021.3130318.

[6] M. S. Khajuee Zadeh, Z. Nasiri-Gheidari, and F. Tootoonchian, "Study of Noise and Vibration in Wound Rotor Resolvers," in *2020 28th Iranian Conference on Electrical Engineering (ICEE)*, IEEE, Aug. 2020, pp. 1–5. doi: 10.1109/ICEE50131.2020.9260668.

[7] H. Lasjerdi, Z. Nasiri-Gheidari, and F. Tootoonchian, "Online Static/Dynamic Eccentricity Fault Diagnosis in Inverter-Driven Electrical Machines Using Resolver Signals," *IEEE Transactions on Energy Conversion*, vol. 35, no. 4, pp. 1973–1980, Dec. 2020, doi: 10.1109/TEC.2020.2996011.

[8] W. Wang, J. Chen, and S. Bi, "A Novel Method for Eliminating Residual Voltage in a Resolver With Signal Fitting Implementation," *IEEE Sens J*, vol. 21, no. 3, pp. 2775–2782, Feb. 2021, doi: 10.1109/JSEN.2020.3027683.

[9] R. Raja, T. Sebastian, M. Wang, A. Gebregergis, and M. S. Islam, "Effect of Position Sensor Error on the Performance of Permanent Magnet Machine Drives," *IEEE Trans Ind Appl*, vol. 53, no. 6, pp. 5518–5526, Nov. 2017, doi: 10.1109/TIA.2017.2704898.

[10] J. Gachter, M. Hirz, and R. Seebacher, "The effect of rotor position errors on the dynamic behavior of field-orientated controlled PMSM," in *2017 IEEE International Electric Machines and Drives Conference (IEMDC)*, IEEE, May 2017, pp. 1–8. doi: 10.1109/IEMDC.2017.8002002.

[11] J. Lara, J. Xu, and A. Chandra, "Effects of Rotor Position Error in the Performance of Field Oriented Controlled PMSM Drives for Electric Vehicle Traction Applications," *IEEE Transactions on Industrial Electronics*, pp. 1–1, 2016, doi: 10.1109/TIE.2016.2549983.

[12] A. Sayed, D. Aliprantis, L. Wu, G. Zhou, and S. Dutta, "Mitigation of DC-Link Voltage Oscillations Caused by Resolver Error in an Electric Vehicle Drivetrain," in *2018 IEEE Energy Conversion Congress and Exposition (ECCE)*, IEEE, Sep. 2018, pp. 3909–3916. doi: 10.1109/ECCE.2018.8557862.

[13] J. Lara, J. Xu, and A. Chandra, "A Novel Algorithm Based on Polynomial Approximations for an Efficient Error Compensation of Magnetic Analog Encoders in PMSMs for EVs," *IEEE Transactions on Industrial Electronics*, vol. 63, no. 6, pp. 3377–3388, Jun. 2016, doi: 10.1109/TIE.2016.2524409.

[14] C. Lian, F. Xiao, J. Liu, and S. Gao, "Analysis and compensation of the rotor position offset error and time delay in field-oriented-controlled PMSM drives," *IET Power Electronics*, vol. 13, no. 9, pp. 1911–1918, Jul. 2020, doi: 10.1049/iet-pel.2019.1115.

[15] N. Abou Qamar, C. J. Hatziadoniu, and H. Wang, "Speed error mitigation for a DSP-based resolver-to-digital converter using autotuning filters," *IEEE Transactions on Industrial Electronics*, vol. 62, no. 2, pp. 1134–1139, Feb. 2015, doi: 10.1109/TIE.2014.2336622.

[16] Shi Wei Zhao, N. C. Cheung, Wai-Chuen Gan, and Jin Ming Yang, "Position Estimation and Error Analysis in Linear Switched Reluctance Motors," *IEEE Trans Instrum Meas*, vol. 58, no. 8, pp. 2815–2823, Aug. 2009, doi: 10.1109/TIM.2009.2016363.

[17] H. Saneie, Z. Nasiri-Gheidari, and F. Tootoonchian, "Design-Oriented Modelling of Axial-Flux Variable-Reluctance Resolver Based on Magnetic Equivalent Circuits and Schwarz–Christoffel Mapping," *IEEE Transactions on Industrial Electronics*, vol. 65, no. 5, pp. 4322–4330, May 2018, doi: 10.1109/TIE.2017.2760862.

[18] F. Totoonchian, "Effect of damper winding on accuracy of wound-rotor resolver under static-, dynamic-, and mixed-eccentricities," *IET Electr Power Appl*, vol. 12, no. 6, pp. 845–851, Jul. 2018, doi: 10.1049/iet-epa.2017.0777.

[19] H. Lasjerdi, Z. Nasiri-Gheidari, and F. Tootoonchian, "Static Eccentricity Fault Diagnosis in Wound-Rotor Resolvers," *IEEE Sens J*, vol. 21, no. 2, pp. 1424–1432, Jan. 2021, doi: 10.1109/JSEN.2020.3019260.

[20] F. Wang, T. Shi, Y. Yan, Z. Wang, and C. Xia, "Resolver-To-Digital Conversion Based on Acceleration-Compensated Angle Tracking Observer," *IEEE Trans Instrum Meas*, vol. 68, no. 10, pp. 3494–3502, Oct. 2019, doi: 10.1109/TIM.2018.2882047.

[21] M. Anwari and A. Hiendro, "New Unbalance Factor for Estimating Performance of a Three-Phase Induction Motor With Under- and Overvoltage Unbalance," *IEEE Transactions on Energy Conversion*, vol. 25, no. 3, pp. 619–625, Sep. 2010, doi: 10.1109/TEC.2010.2051548.

[22] S. Ahmed, C. Grabher, H.-J. Kim, and T. Koseki, "Multifidelity Surrogate Assisted Rapid Design of Transverse-Flux Permanent Magnet Linear Synchronous Motor," *IEEE Transactions on Industrial Electronics*, vol. 67, no. 9, pp. 7280–7289, Sep. 2020, doi: 10.1109/TIE.2019.2945302.

[23] C. Zhang *et al.*, "A computationally efficient surrogate model based robust optimization for permanent magnet synchronous machines," *IEEE Transactions on Energy Conversion*, pp. 1–1, 2022, doi: 10.1109/TEC.2021.3140096.

[24] M. Salameh, S. Singh, S. Li, and M. Krishnamurthy, "Surrogate Vibration Modeling Approach for Design Optimization of Electric Machines," *IEEE Transactions on Transportation Electrification*, vol. 6, no. 3, pp. 1126–1133, Sep. 2020, doi: 10.1109/TTE.2020.3017232.

[25] X. Ge and Z. Q. Zhu, "A Novel Design of Rotor Contour for Variable Reluctance Resolver by Injecting Auxiliary Air-Gap Permeance Harmonics," *IEEE Transactions on Energy Conversion*, vol. 31, no. 1, pp. 345–353, Mar. 2016, doi: 10.1109/TEC.2015.2470546.

[26] Yashan Hu, Zi-Qiang Zhu, and Kan Liu, "Current Control for Dual Three-Phase Permanent Magnet Synchronous Motors Accounting for Current Unbalance and Harmonics," *IEEE J Emerg Sel Top Power Electron*, vol. 2, no. 2, pp. 272–284, Jun. 2014, doi: 10.1109/JESTPE.2014.2299240.